





Listening to Radiation Damage In Situ: Passive and Active Acoustic Techniques

CODY A. DENNETT ^{1,4} R. CHARLES CHOENS,² CAITLIN A. TAYLOR,²
NATHAN M. HECKMAN,² MATHEW D. INGRAHAM,²
DAVID ROBINSON,³ BRAD L. BOYCE,² MICHAEL P. SHORT ^{1,5} and
KHALID HATTAR^{2,6}

1.—Department of Nuclear Science and Engineering, Massachusetts Institute of Technology, Cambridge, MA 02139, USA. 2.—Sandia National Laboratories, Albuquerque, NM 87185, USA. 3.—Sandia National Laboratories, Livermore, CA 94551, USA. 4.—e-mail: cdennett@mit.edu. 5.—e-mail: hereiam@mit.edu. 6.—e-mail: khattar@sandia.gov

Knowing when, why, and how materials evolve, degrade, or fail in radiation environments is pivotal to a wide range of fields from semiconductor processing to advanced nuclear reactor design. A variety of methods, including optical and electron microscopy, mechanical testing, and thermal techniques, have been used in the past to successfully monitor the microstructural and property evolution of materials exposed to extreme radiation environments. Acoustic techniques have also been used in the past for this purpose, although most methodologies have not achieved widespread adoption. However, with an increasing desire to understand microstructure and property evolution in situ, acoustic methods provide a promising pathway to uncover information not accessible to more traditional characterization techniques. This work highlights how two different classes of acoustic techniques may be used to monitor material evolution during in situ ion beam irradiation. The passive listening technique of acoustic emission is demonstrated on two model systems, quartz and palladium, and shown to be a useful tool in identifying the onset of damage events such as microcracking. An active acoustic technique in the form of transient grating spectroscopy is used to indirectly monitor the formation of small defect clusters in copper irradiated with self-ions at high temperature through the evolution of surface acoustic wave speeds. These studies together demonstrate the large potential for using acoustic techniques as in situ diagnostics. Such tools could be used to optimize ion beam processing techniques or identify modes and kinetics of materials degradation in extreme radiation environments.

INTRODUCTION

Materials subject to high levels of radiation exposure may experience drastic changes in their structure and properties. Over long periods, these changes may lead to degradation and eventual component failure in systems including nuclear power reactors^{1,2} and space systems.^{3,4} Radiation-induced changes may also be used as a forensic tool in either accident scenarios or nuclear security applications to determine the environments to which materials have been exposed.⁵ Targeted applications of radiation have been used as

nanoscale device processing tools for decades, most notably in the semiconductor industry.⁶ In these contexts and many others, reliably characterizing radiation-induced effects on both the structure and properties of many classes of materials is a vital challenge.

A wide variety of tools have been used to conduct post-irradiation examination (PIE) depending on the radiation-induced effect under investigation. Standard techniques involve tensile testing to characterize radiation-induced hardening,^{7–9} Charpy impact testing to characterize embrittlement,^{10,11} transmission electron microscopy (TEM) to directly

characterize defect type and density,^{12,13} and analytical electron and x-ray techniques to map radiation-induced segregation or precipitation,^{14–16} among many others. Challenges often arise when seeking to investigate materials which have been subject to direct neutron exposure due to hazards arising from sample activation. Although these conditions may most directly emulate those seen in service conditions, laboratory investigations using neutrons are often impractical to implement due to this activation, as well as the limited availability of neutron sources (e.g., reactors or spallation sources). Ion beam irradiation is commonly utilized to simulate the radiation-induced evolution expected under service conditions, as ion beams are readily available, more flexible in their implementation, and can result in little to no material activation.^{17,18} Thus, ion beam irradiation is the tool of choice when seeking to rapidly screen new materials being proposed for use in nuclear systems.

Despite the advantages offered by ion beam irradiation, new challenges are encountered due to the limited penetration depth of charged ions compared to neutrons. This limited range severely reduces the total volume of damaged material available for examination and has spurred the development of specialized techniques for PIE of ion-damaged materials. Microscopy techniques seeking to evaluate meaningful defect distributions and densities will often restrict analysis to specific layers only hundreds of nanometers thick from bulk implanted samples.^{19,20} Specialized nanomechanical testing schemes have also been developed—pillar compression, push–pull tensile testing, nanoindentation, notch testing, and more—to attempt to recover bulk material properties from these small volumes.^{21–25}

One class of underexplored methodologies of particular interest for the characterization of radiation-induced changes is acoustics. Broadly, these methods are concerned with the properties of elastic wave propagation through solid materials. The speeds at which acoustic waves propagate, the degree to which they are attenuated, and their non-linearities can all be used to determine information about the material properties and damage structure. Methods of ultrasonic characterization have been used for some time as PIE tools on materials exposed to various levels of radiation. For example, Matlack et al. used acoustic non-linearities to study embrittlement in reactor pressure vessel steels and were able to correlate changes to specific defect populations.^{26,27} Etoh and coworkers used contact ultrasonics to map porosity evolution in stainless steel exposed to high levels of neutron irradiation.²⁸ Duncan and coworkers tracked anisotropic changes in acoustic wave velocities in single-crystal tungsten implanted with helium to confirm the presence of oriented He-vacancy complexes.^{29,30}

Finally, Dennett et al. correlated changes in acoustic wave velocity to volumetric void swelling in copper self-ion irradiated at high temperature.³¹

Although much has been gained from the wealth of available PIE methods, the limited snapshots in dose often mean that transient microstructures and subsequent properties can be easily overlooked. In situ measurements during ion irradiation permit the continuous observation of microstructure, properties, and system characteristics throughout the experiment, shedding light on these transient features. For example, the ability to measure the electrical performance of devices during ion irradiation is mature and used in many laboratories.³² In addition, efforts have been undertaken by several ion beam laboratories to understand the structural evolution through a combination of in situ TEM or Raman spectroscopy.^{33–36} An even smaller effort has explored the evolution of thermal and mechanical properties during ion bombardment.^{37–40} Efforts are ongoing in the field at a variety of laboratories to incorporate scanning tunneling microscopy, scanning electron microscopy, and even positron annihilation spectroscopy into ion beam end stations to provide greater insight into chemical, microstructural, and property evolution as a function of radiation damage.

Given both the flexibility in implementation and the ability to evaluate material properties and damage structures non-destructively, acoustic testing is increasingly being used in this new generation of in situ monitoring techniques. By “listening” to a material as it is being exposed to extreme radiation environments, a time-resolved record of property evolution and damage events may be recovered.

In this work, we explore two different listening modalities and how each may be used in the context of radiation effects. First, acoustic emission (AE) testing, a passive listening technique, may be used to track the incidence and location of certain damage events induced by radiation. Stress-relief events such as cracking and blistering may emit transient elastic waves which can be detected and monitored using contact ultrasonic transducers. Using a network of sensors, the arrival times of the elastic waves can be used to localize the source of the event in real time,^{41–43} although such localization has not been implemented in this work. AE monitoring has been used in a limited number of irradiation studies in the past, primarily focusing on low (100s of keV⁴⁴) or extremely high (single GeVs^{45,46}) energy ion implantation. Here, we focus on moderate energy ions (single MeVs) such that we primarily listen to damage accumulation in a microns-thick surface layer. This method is classed as passive, as no external stimulus is necessary to generate the effect measured. Samples acoustically emitting in this manner will produce signatures in these environments whether or not a sensor is affixed.

In contrast, a second class of active listening techniques which rely on an external input of energy may also be applied to track fine changes in material properties during radiation exposure. In this category, we use a photoacoustic methodology known as transient grating spectroscopy (TGS) to induce and monitor surface acoustic waves on materials as they are being exposed to radiation. By providing an impulse of energy from a pulsed laser, short-lifetime acoustic waves are excited and their oscillation monitored as they decay.^{47,48} The properties of these acoustic waves may be measured at extremely high resolution in this manner. These excitations decay on the timescale of tens of nanoseconds, often much faster than damage is accumulated, providing a snapshot in time of the material properties at each excitation. Recently, an in situ ion beamline at Sandia National Laboratories was commissioned which is dedicated to this type of continuous characterization.⁴⁹

Here, these two methodologies—AE and TGS—will each be described in detail. A series of in situ AE experiments are conducted on a model ceramic (quartz) and face-centered cubic (FCC) metal (palladium) exposed to 2 MeV helium ion implantation to demonstrate the utility of this passive technique on a variety of material systems. In situ TGS experiments are conducted on a model FCC metal (copper) during self-ion irradiation at high temperature. These tests demonstrate the utility of active listening at combined extremes of radiation exposure and temperature.

PASSIVE AND ACTIVE LISTENING TECHNIQUES

Passive acoustic sampling relies on energy releases from rapid stress relaxation events within materials. These events may occur when stresses are induced on a specimen through any number of means. Classic examples of stress relaxation events include cracking, grain boundary debonding, and phase transformations induced by external loading.^{50–53} This technique has been used in geomechanics and civil engineering⁵⁴ to monitor failure processes and map fracture growth in a number of different rock types,^{41,55,56} geomaterials,^{42,43,57,58} and concrete.^{59–62}

AE monitoring involves coupling a piezo-electric crystal, or crystals, to the sample using an adhesive or acoustic couplant. When a propagating elastic wave strikes the piezo, the deformation generates a small electric signal that is magnified using in-line preamplifiers and recorded with high-speed digital oscilloscopes. With a multi-channel system, multiple waveforms arriving in short succession can be used to locate individual acoustic events within the sample by using the difference in the arrival times at the different sensors. Uncertainty in these measurements is decreased by increasing the number of

sensors on a sample; as the number of sensors increases, tomographic reconstruction of damage events becomes possible.⁶³

The AE data from in situ ion beam irradiation in this work were recorded with a single Dynasen 0.093" diameter piezo-electric transducer (model CA-1163) as proof-of-principle experiments. Side- and front-view schematics of the in situ AE experimental configuration are shown in Fig. 1a and b, respectively. The transducer pin was electrically insulated, slotted into an aluminum mounting block, and pressed flush against the back side of the sample. Silicone-based vacuum grease was used as an acoustic couplant. Samples were affixed to the mounting block using a series of mounting clips, centered on the pin. During irradiation, the ion beam spot was steered to the center of the sample, aligned with the transducer pin. A Mistras Micro-II Express system with an Express-8 eight channel AE board was used to monitor and record AE. This system is capable of filtering, recording, and analyzing AE hits as well as collecting individual waveforms. Signals were amplified by 60 dB with an in-line preamplifier and bandpass filtered for a range of 200 kHz to 1 MHz. With this Mistras system, an AE hit is recorded when the signal crosses a user-defined trigger threshold. The maximum signal amplitude able to be registered is 100 dB; no AE hits recorded in this work reached that limit. Only a single transducer was used in this scoping study, requiring the use of only a single channel on the Mistras system. This configuration was the simplest to implement given the small size of the samples and the constraints of the multi-purpose ion beam target chamber. Nonetheless, these initial point measurements demonstrate the utility of the AE methodology applied during irradiation.

In contrast to the relatively simple-to-implement passive listening technique, active acoustic interrogation is accomplished through the use of the dedicated in situ ion irradiation transient grating spectroscopy (I^3 TGS) beamline at Sandia National Laboratories. This facility is described in detail in a recent work.⁴⁹ The transient grating method operates by exciting surface acoustic waves (SAWs) and a one-dimensional (1D) transient temperature profile with a well-defined wavelength on the sample under interrogation. This excitation is generated by crossing two laser pulses with durations of tens to hundreds of picoseconds at a known angle at a sample's surface, projecting a 1D interference pattern. The standard TGS implementation generates both of these excitation pulses from a single source by splitting a pulsed laser with a volumetric diffraction optic and recombining the ± 1 diffraction orders as the excitation pair.^{47,64} This geometry, the same as that implemented on the I^3 TGS beamline, can be used to reliably generate single-wavelength excitations with periods in the range of 1–100 μm over

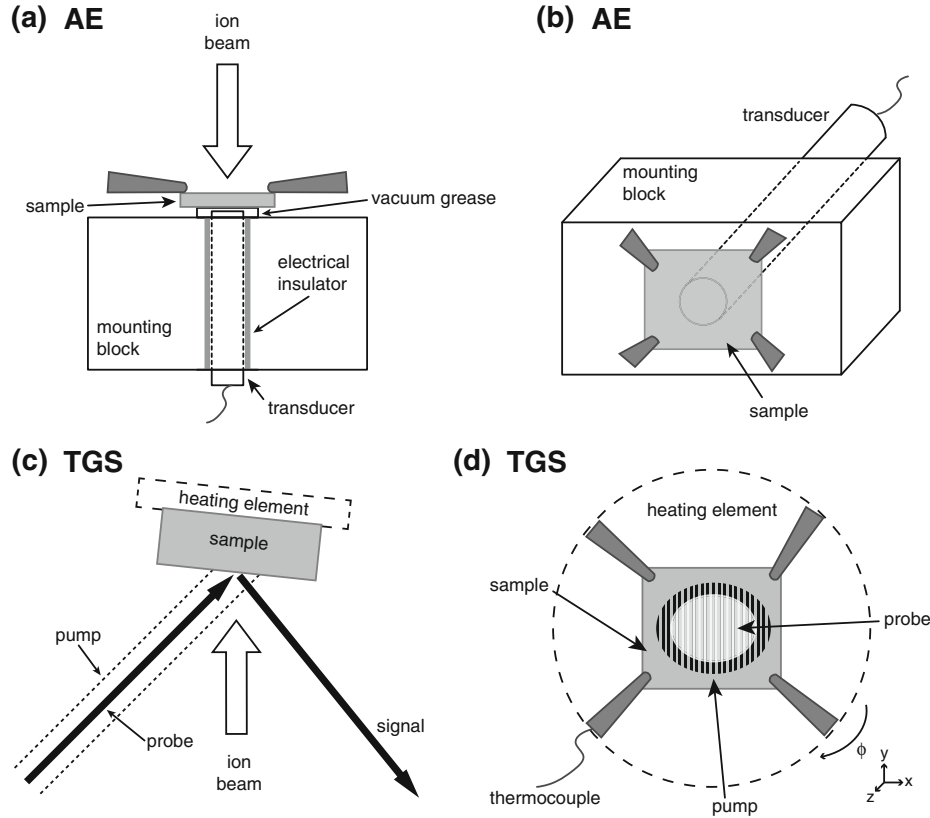


Fig. 1. (a) Side and (b) front views of in situ AE ion irradiation experiments. The acoustic transducer is electrically insulated and set in a thermally-conductive mounting block. Samples are clipped to the transducer surface over a layer of vacuum grease to ensure effective coupling. (c) Top and (d) front views of in situ ion irradiation TGS. Samples are affixed directly to a high-temperature sample manipulator using a series of clips. A sample surface is excited (pumped) with a periodic laser intensity profile and the resulting excitations are monitored using a continuous wave probing laser placed inside the excited spot.

spot sizes of several hundred microns. For in situ experiments, excitations with wavelengths from $4\ \mu\text{m}$ to $10\ \mu\text{m}$ and spot sizes of $\sim 200\ \mu\text{m}$ can be generated with a laser energy of $5\ \mu\text{J}$ applied over a $400\ \text{ps}$ pulse at $532\ \text{nm}$ and a repetition rate of $1\ \text{kHz}$.

To monitor the oscillation and decay of the induced acoustic wave(s), a quasi-continuous wave probing laser is directed into the center of the excited region. The periodic surface displacement associated with the SAW acts as a diffraction optic for this probe laser. By recording the diffracted intensity of this beam, the dynamics of the excitation may be monitored. In practice, an optical heterodyne amplification scheme is implemented to allow SAWs excited with very small amplitudes to be reliably detected.⁴⁷ In this work, the probing laser used is a $785\ \text{nm}$ narrow line-width CW laser modulated with a 25% duty cycle at the pump laser repetition rate of $1\ \text{kHz}$. The total probing laser intensity at the sample surface is $10\text{--}15\ \text{mW}$. Analytical models have been developed to extract both acoustic and thermal transport property data from TGS measurements.^{64–66} Acoustic wave frequencies and in-plane thermal diffusivity are measured

directly, and the acoustic wave speeds can be calculated from those frequencies and the measured projected fringe spacing.

Figure 1c and d show, respectively, top- and front-view schematics of the experimental geometry used in the I³TGS system. For in situ irradiations, the sample is placed at a slightly off-normal incidence to the ion beam to reduce the effects of ion channeling in single-crystal samples.⁴⁹ The TGS laser excitation is generated outside the high vacuum target chamber and placed incident onto the sample surface at about 45° to that surface. In this geometry, the diffracted signal of interest is then reflected along the corresponding 45° on the other side of the chamber. That diffracted intensity is monitored on Si avalanche photodiodes with a bandwidth of $1\ \text{GHz}$ recorded by a $5\ \text{GHz}$, dual-band digital oscilloscope. Samples are affixed using a series of mounting clips to a high-temperature resistive heating element prior to being placed in the measurement position. One of the mounting clips has a thermocouple welded to the tip for temperature feedback and control. Figure 1d depicts a sample mounted to the heating element, with both the 1D excitation laser spot and probing laser spot shown (not to scale).

Table I. Comparison of the passive (AE) and active (TGS) acoustic techniques used in this study

Technique	AE	TGS
Temperature	Cryo to high	Cryo to high
Surface quality	Any	Mirror
Irradiation conditions	Any	Any
Dimensionality	3D	2D
Resolution	Millimeters	Microns
Ease of use	Easy	Difficult
Contact needed?	Yes	No
Frequency spectrum	Broad	Monochromatic
Grain size	Any	Large/ultrafine

Temperature ranges, dimensionality, and spatial resolution refer to qualities previously demonstrated, although not all have been demonstrated in situ during ion beam irradiation.

While stress relaxation events may be directly monitored in AE to elucidate damage mechanisms, SAW monitoring in TGS relies on detecting small changes in material properties due to changes in microstructure induced by radiation. Such changes in elastic properties have been attributed to purely point defect concentrations⁶⁷ and larger-scale accumulated damage from continuous exposure.^{29–31} In either case, foreknowledge of expected defect effects on acoustic characteristics allows for highly-resolved records of radiation-induced material evolution to be generated in situ.

Taken together, these two methodologies provide a set of experimental techniques which may be applied as in situ diagnostics in a variety of circumstances. Table I provides a comparison of the two techniques in terms of characteristics to consider when designing experiments for solid, opaque samples. Given the overall complexity of the systems necessary for each type of testing, AE is classed as relatively easy to implement in the form we describe here, whereas in situ TGS experiments require significant preparation to successfully complete. Of particular note is the mirror-polished surface required for reflective TGS measurements, while AE samples may have any surface quality. At present, both methods have been implemented in situ as single point measurements. However, in principle, AE testing could be used for three-dimensional event localization and TGS can be used to generate two-dimensional maps of evolving properties across material surfaces. Finally, acoustic data from TGS experiments on materials with grain sizes on the order of 10s to 100s of microns, close to the excitation spot size may be difficult to interpret, as the elastic anisotropy of most materials may cause SAWs with multiple velocities to be excited simultaneously on neighboring grains. The presence of multiple SAW velocities drastically increases the difficulty of tracking small changes in these velocities to infer microstructure evolution. AE testing, in contrast, is minimally affected by grain to grain variations.

In the following sections, recent results from both in situ AE and TGS testing are discussed. These experiments cover a wide range of material morphologies, classes, and exposure conditions to show that acoustic interrogation is indeed a powerful tool to study radiation-induced material evolution.

IN SITU ACOUSTIC EMISSION MONITORING

In this work, one sample of palladium foil and two quartz crystal samples were exposed to interrupted ion bombardment from a 2 MeV He⁺ beam while undergoing continuous AE monitoring. Each sample was larger than the cross-section of the AE transducer such that the ion beam could not impinge directly on the pin. Both materials used for these proof-of-principle tests were legacy samples available in the laboratory with unknown thermal histories, and received no preparation prior to being mounted as shown in Fig. 1a. For the palladium exposure, the average applied beam current was 350 nA over a spot size of approximately 2 mm in diameter. For the quartz experiments, the average applied beam current was 3.6 nA over the same ~ 2 mm spot. With 2 MeV He⁺ ions, the resulting damage layers were approximately 2.9 μm and 5.9 μm thick for Pd and quartz, respectively, as calculated using SRIM and literature displacement energies.^{68–70}

Samples were exposed at room temperature with no active cooling to compensate for local heating from the ion beam. Interrupted exposures were conducted by dropping a Faraday cup into the path of the ion beam upstream of the target chamber once the desired fluence level was achieved in each individual exposure event. Fluence levels in each of the events were measured by collecting charge on a beam chopper upstream of the target chamber with a known duty cycle and frequency. The single palladium sample was exposed to a total fluence of 2.1×10^{17} ions/cm² over the course of three exposure events, the first quartz sample to 1.1×10^{15} ions/cm² during two exposure events (low dose), and the second quartz sample to 2.0×10^{15} ions/cm² over 13 exposure events (high dose). Table II describes the fluence levels applied during each individual exposure event and gives each of these events a 6-character exposure ID of the form (Material)(Sample Number)(Exposure Number). These IDs will be used in the following discussion to describe the observed AE events induced by the ion beam.

For the Pd sample, a 33 dB trigger threshold was used for PD0101 and PD0102, and a 32 dB threshold was used for PD0103. All quartz exposures were recorded at a 20 dB threshold, but the value was raised to 30 dB in postprocessing to remove noise. Waveforms were recorded at a 10 MHz sampling rate, leading to a temporal resolution of 0.1 μs . For experiments with Pd, the conductive sample

Table II. Applied He⁺ ion fluence levels during each shot of the in situ AE tests

Material	Sample no.	Exposure no.	He ⁺ Fluence (ions/cm ²)	ID
Pd	1	1	1×10^{16}	PD0101
	1	2	1×10^{17}	PD0102
	1	3	1×10^{17}	PD0103
		Total	2.1×10^{17}	
Quartz	1	1	1×10^{14}	QZ0101
	1	2	1×10^{15}	QZ0102
		Total	1.1×10^{15}	
Quartz	2	1	1×10^{14}	QZ0201
	2	2	1×10^{14}	QZ0202
	2	3	1×10^{14}	QZ0203
	2	4	1×10^{14}	QZ0204
	2	5	1×10^{14}	QZ0205
	2	6	1×10^{14}	QZ0206
	2	7	1×10^{14}	QZ0207
	2	8	1×10^{14}	QZ0208
	2	9	1×10^{14}	QZ0209
	2	10	1×10^{14}	QZ0210
	2	11	3×10^{14}	QZ0211
	2	12	5×10^{14}	QZ0212
	2	13	2×10^{14}	QZ0213
		Total	2.0×10^{15}	

Exposure IDs are used when describing specific observed AE events.

resulted in the AE transducer being in weak electrical contact with the sample mounting block through the thin film of vacuum grease. Electrical background noise on the sensor once in the chamber presented a data collection issue, but grounding, filtering, and high threshold values eliminated background electrical noise from triggering false hits. Little to no AE was recorded when the Faraday cup was obstructing the beam from the sample, suggesting that the observed AE resulted from the ion beam exposure.

Palladium Acoustic Emissions

A total of 14 AE hits were observed in the palladium foil, 2 hits during PD0101, 11 hits during PD0102, and 1 hit during PD0103 (Fig. 2a). The first 2 hits were short, moderately-high-amplitude events (Fig. 2b). In PD0102, events were a mix of short and long durations, with the highest amplitudes observed for palladium (Fig. 2b). One extremely long duration event was observed that lasted 726 μ s; all other events were less than 110 μ s. During PD0103, only a single short-duration, medium-amplitude hit was recorded (Fig. 2b) despite the lower trigger

threshold. Finally, an additional hit was observed shortly after the Faraday cup was closed (Fig. 2a).

Classically, hit amplitude and duration can be helpful tools in determining damage mechanisms. High-amplitude, short-duration events are typically associated with impulse deformation, like the opening of a tensile crack. Longer duration, ringing events are created by persistent deformation, like slip along a shear fracture.^{61,62} Under ion beam exposure, samples will be deforming at the microstrain level by penetrating He⁺ ions. Hits could be caused by movement of dislocations, generation of new dislocation sources, coalescences of dislocation into bubbles, phase transitions, gas accumulation and transmission, and crack nucleation and propagation.^{44,71-74} The limited number of observed AE hits makes it difficult to differentiate between deformation mechanisms, but the results show at least two different mechanisms corresponding to short duration and long duration hits.

Preliminary microstructure analysis revealed several features which may be responsible for the observed AE. TEM investigation following focused ion beam (FIB) lift-out showed a number of pre-existing cavities in the rolled palladium foil. Micrographs of the peak implantation region, Fig. 2c and d, shows both these cavities as well as helium bubbles induced via ion implantation. These bubbles have an average diameter of 1.5 nm and appear over a depth range of 584 nm around the implantation peak.⁶⁸ These bubbles were first observed at a depth of 2.7 μ m into the sample surface, corresponding to a helium concentration 2.4 at% at this implantation energy and fluence. Some cracking of the foil is also observed in the near-surface region, likely concentrated around pre-existing cavities.

Further investigation of the as-damaged microstructure is necessary before a definitive correlation may be drawn between the observed defect and failure modes and the particular AE signatures recorded during exposure. Given the presence of two distinct damage/failure modes, the short hit-duration mechanism is likely related to the generation of these bubbles and the higher amplitude hits are likely related to the more severe deformation associated with cracking at or near the surface. An analysis comparing the energy theoretically released for each of these two damage modes to that recorded with AE may help in making that differentiation.⁷⁵

Quartz Acoustic Emissions

Substantially higher AE activity was observed in quartz, despite a two order of magnitude reduction in ion fluence compared to the palladium exposure. A total of 3467 hits were recorded during testing for the first quartz sample, and 19,548 hits were recorded in the second quartz test (Fig. 3a and c). For the first wafer, AE rates remained around 50 hits/s. For the second wafer, AE rates varied

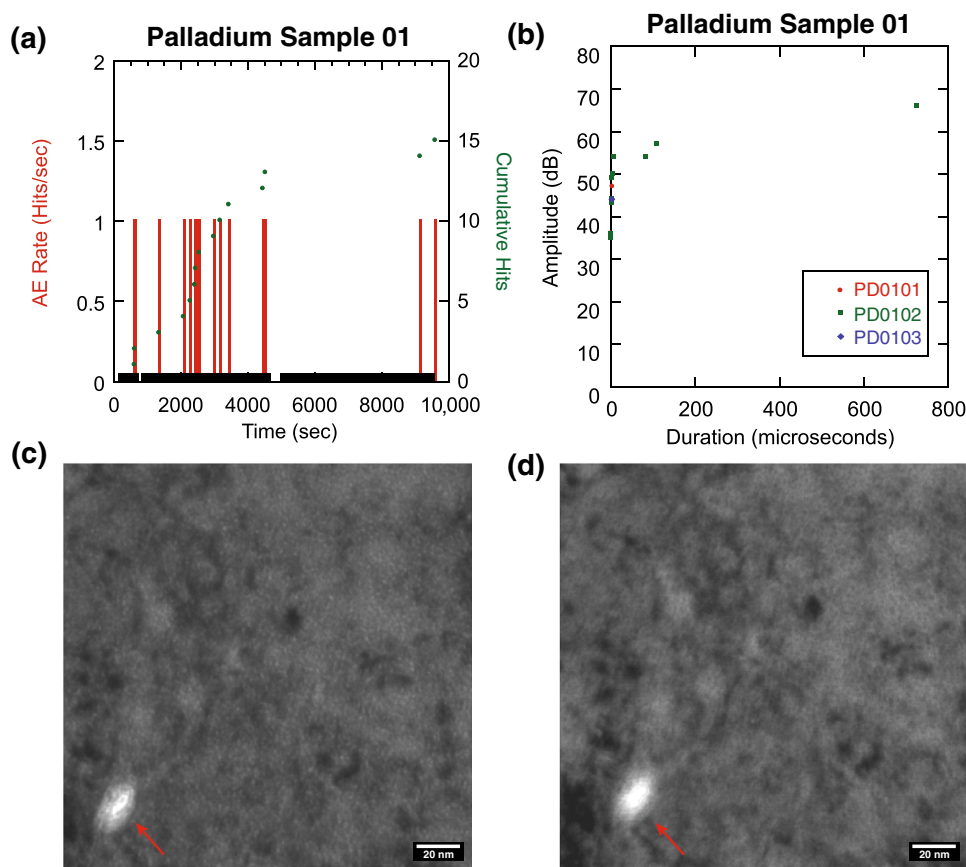


Fig. 2. Measured AE activity in palladium foil under ion beam exposure. (a) AE rate and cumulative AE hits versus time for the three ion beam exposures. The black bar along the x-axis represents exposure events. (b) Amplitude versus duration for AE hits from the three different exposure events. Transmission electron micrographs of the peak implanted region in Pd using (c) under- and (d) over-focused Fresnel imaging conditions. Small helium bubbles, 1.5 nm in diameter on average, are observed as light in the under-focused and dark in the over-focused image. The red arrows indicate a pre-existing cavity in the foil.

greatly, ranging from 10 to 260 hits/s. AE rates were highest during QZ0201, QZ0208, and QZ0213. Observed amplitudes ranged from 30 dB to 77 dB, and durations ranged from 1 μ s to 649 μ s (Fig. 3b and d).

During QZ0102, AE stopped after the first 100 seconds into that exposure. Visual inspection showed the sample had fractured at the ion beam spot location. The second wafer did not fracture despite the higher total ion exposure, suggesting that fracture most likely occurred due to thermal expansion at the beam location from the long continuous exposure. Thermal expansion prior to cracking could have warped the sample away from the AE sensor, or the elevated temperature could have interfered with the vacuum grease, disrupting the acoustic coupling and preventing recording of subsequent fracturing. On the second wafer, shorter exposure steps prevented overheating and thermally-induced cracking.

For the low-dose quartz sample, AE hits can be divided into three groups (Fig. 3b). The majority of hits are relatively short duration with amplitudes varying between 30 dB and 70 dB. There are also a number of hits with amplitudes around 70 dB with

durations from 100 μ s to 400 μ s. The third group of hits has amplitudes of 30–45 dB with medium duration. Inspection of waveforms from this latter group shows that many of these hits are multiple short hits in quick succession on one recording, suggesting that total AE is undercounted and that durations for this group are exaggerated.

AE hits for the high-dose quartz sample can be divided into similar groupings as the first: short-duration events with amplitudes ranging from 30 dB to 76 dB, long-duration events up to 649 μ s in length, and, in the third group, medium amplitudes from 30 dB to 55 dB with durations exceeding 400 μ s (Fig. 3d). A temporal evolution in AE can be observed through the different exposure events. The long-duration hits over 200 μ s with amplitudes around 70 dB all occur in the first three exposures, QZ0201–03. For QZ0204–06, hits are all short duration. For later exposures, an increasing number of hits are the third category of low to moderate amplitude with medium durations. QZ0211 has a number of hits at 70 dB with durations less than 200 μ s, as well as a number of hits at amplitudes from 50 dB to 60 dB with durations as long as 400 μ s. The final exposure, QZ0213, results in

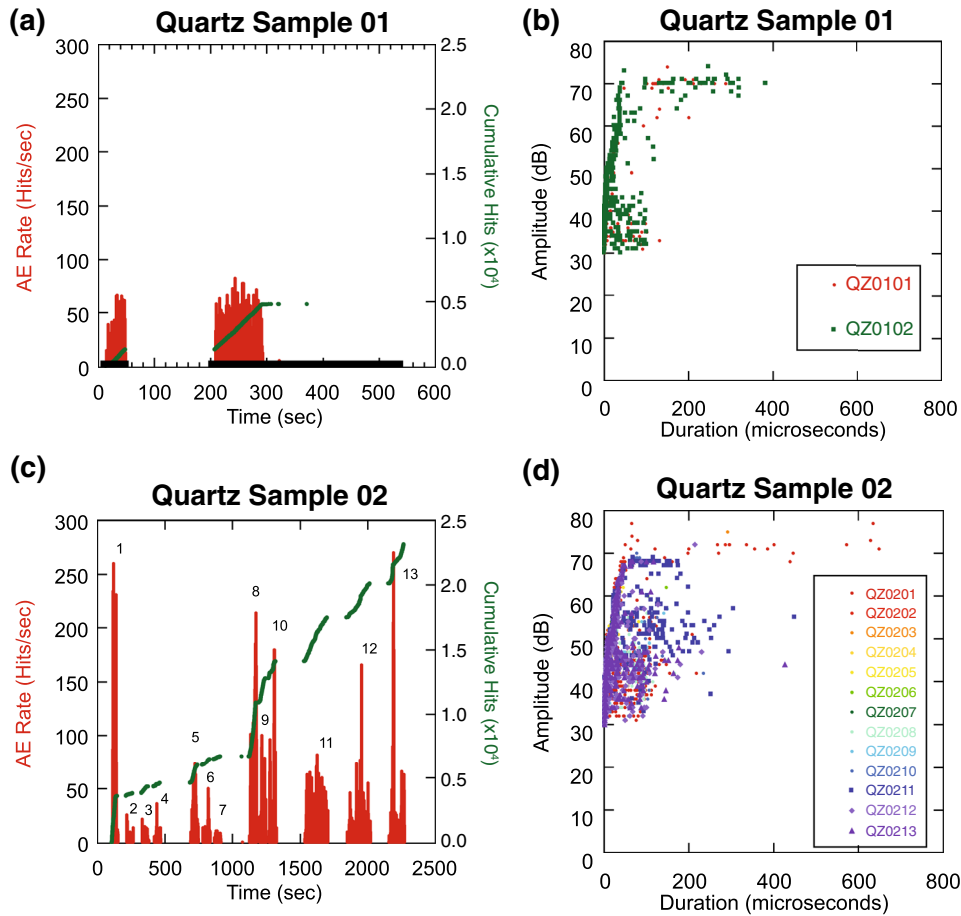


Fig. 3. Measured AE activity in two quartz wafers under ion beam exposure. (a) First quartz sample AE rate and cumulative AE hits versus time for the two ion beam exposures. The black bar along the x-axis represents exposure events. (b) First quartz sample amplitude versus duration for AE hits from the two different exposure events. (c) Second quartz sample AE rate and cumulative AE hits versus time for the 13 ion beam exposures. Individual exposure events are numbered. (d) Second quartz sample amplitude versus duration for AE hits for all exposure events.

primarily short-duration hits (Fig. 3d). While the frequencies of measured events is imperceptible to humans, reducing the speed of events by a factor of 1000 allows for an audible comparison. Some examples are presented in digital supplementary sound files for events with high- and low-amplitude hits, where both single and multiple pulses were recorded. These combinations represent the different types of events observed during irradiation. Supplementary file names correspond to the amplitude and length of the event and all amplitudes have been normalized for playback.

The amplitude versus duration plots (Fig. 3b and d) for the two different quartz samples are similar, despite the fact the first sample cracked midway through exposure. This suggests that the same deformation mechanisms were active in the two different tests. It also suggests that the AE associated with macroscopic cracking for the first quartz sample was either not recorded or obscured by other AE hits. Further investigation is necessary to confirm the particular deformation mode associated with the AE hits recorded in these experiments. However, given the relatively large acoustic output,

the act of ‘going quiet’ as observed in the low-dose sample (when AE ceased during exposure) may be an extremely powerful tool in and of itself when using ion beams to purposely decouple layers from a surface (e.g., cleavage during wafer processing).

IN SITU TRANSIENT GRATING SPECTROSCOPY

To demonstrate active acoustic interrogation, a series of in situ TGS experiments were conducted on pure, single-crystal copper. Copper crystals with dimensions $5 \times 5 \times 1$ mm and {111} surface orientation were purchased from the MTI Corporation. Samples are >99.999% pure, mechanically polished to <3 nm surface roughness, and have surface orientations within 2° of the given index. These samples were chosen to extend the previous ex situ TGS work which was conducted on self-ion irradiated copper.³¹ In that study, copper samples exposed at high temperatures were shown to exhibit microstructure evolution which could be correlated to changes in SAW speeds across all polarizations on a {111} surface. For in situ experiments, only one acoustic polarization may be sampled continuously

during irradiation. As Dennett et al. previously found that the $\langle 11\bar{2} \rangle \{111\}$ polarization showed the largest absolute changes in SAW speed,³¹ copper crystals were aligned roughly at this polarization for these exposures. Samples were exposed to 31 MeV Cu^{5+} ions such that the thickness of the damaged surface layer matches the depth to which properties are sampled at the applied excitation wavelength of 4.5 μm .^{31,49} Three in situ exposures were conducted at 400°C, 425°C, and 475°C. Following a 20 min to 40 min temperature ramp from room temperature, each sample is held for a soak of ~ 20 min—during which baseline measurements are recorded—prior to high-temperature exposure with temperatures stable within $\pm 0.5^\circ\text{C}$ of the set point. The motivation for varying the exposure temperature will be discussed below. During each exposure, a spinning-wire beam profile monitor calibrated to a Faraday cup upstream of the target chamber is used to continuously record the applied ion beam current. TGS measurements were collected as averages over many individual laser shots in batches of 35 s at 60 second intervals throughout each exposure. Relevant parameters for each in situ TGS experiment are listed in Table III.

Previously, Dennett and coworkers noted that in this range of experimental conditions, pure copper will readily undergo volumetric void swelling. Ex situ TGS testing revealed that, at low exposure levels, the SAW velocity is observed to increase with increasing dose before turning over and decreasing at high dose levels.³¹ This low-dose stiffening effect is attributed to an interaction mechanism between small radiation-induced defect clusters and a native dislocation network in the crystal matrix, which increases the effective elastic modulus of the material, increasing the measured SAW velocity.^{76–80} Sufficient porosity generated due to void swelling serves to reverse this trend and causes the SAW velocity to decrease at high doses.⁸¹

The initial irradiation conducted in this series used the previous work's set-point temperature of 400°C in an attempt to re-create this stiffening-followed-by-softening effect directly. Although exposed to a total dose of 95 displacements per atom (dpa) at the damage peak (a fluence of 6.7×10^{16} ions/cm²), the SAW velocity was observed to increase steadily and then saturate, rather than decrease in the high-exposure regime. As a result,

two additional exposures were conducted at 425°C to a total dose of 127 dpa (8.9×10^{16} ions/cm²) and 475°C to a total dose of 99 dpa (7.0×10^{16} ions/cm²). Both of these exposures showed the same trend, an increase in SAW velocity with exposure level which never reversed and began to soften as void swelling occurred. Time-resolved TGS-measured SAW velocities for all three experiments are shown in Fig. 4. One feature of note is that, although all three experiments are conducted along the same surface polarization, the initial SAW velocity decreases as a function of exposure temperature. This effect is due to the expected reduction in the effective elastic modulus at high temperature.

The data in Fig. 4 clearly do not meet the expectations set by previous experiments on the

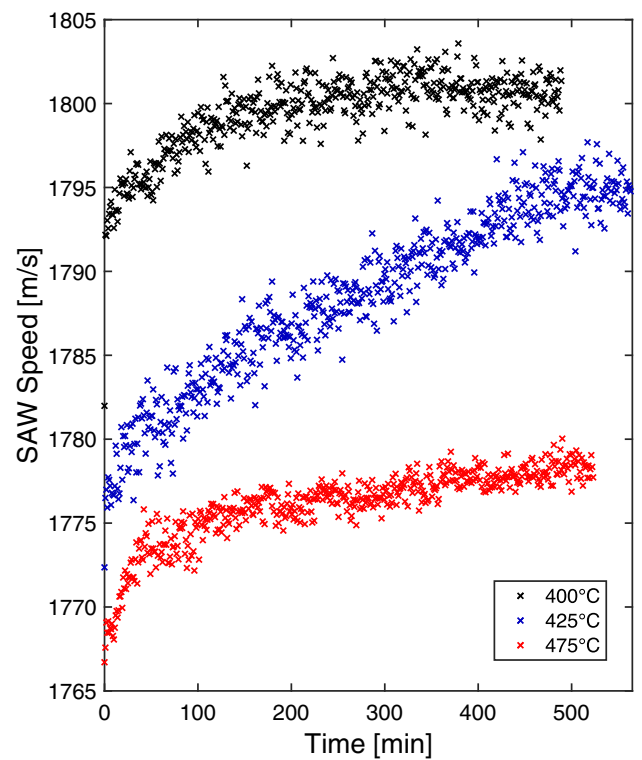


Fig. 4. Evolution of SAW velocity as a function of exposure time for each of the Cu self-ion irradiations. For all temperatures, SAW velocities increase with increasing exposure, with some saturation behavior evident. Differences in initial SAW velocities as a function of temperature are consistent with temperature-dependent changes in elastic modulus.

Table III. In situ TGS exposure parameters for the single crystal (SC) pure copper sample matrix

Material	Surface polarization	Ion species	Ion energy	Temp.	Spot diameter	Avg. beam current	Meas. time	Meas. interval
SC Cu	$\sim \langle 11\bar{2} \rangle \{111\}$	Cu^{5+}	31 MeV	400°C	1.8 mm	44 nA	35 s	60 s
SC Cu	$\sim \langle 11\bar{2} \rangle \{111\}$	Cu^{5+}	31 MeV	425°C	2.2 mm	80 nA	35 s	60 s
SC Cu	$\sim \langle 11\bar{2} \rangle \{111\}$	Cu^{5+}	31 MeV	475°C	2.0 mm	56 nA	35 s	60 s

Spot diameter refers to the measured ion beam spot size in the sample plane. The continuously-monitored ion beam current is averaged over the time of exposure to generate the *Avg. beam current* column.

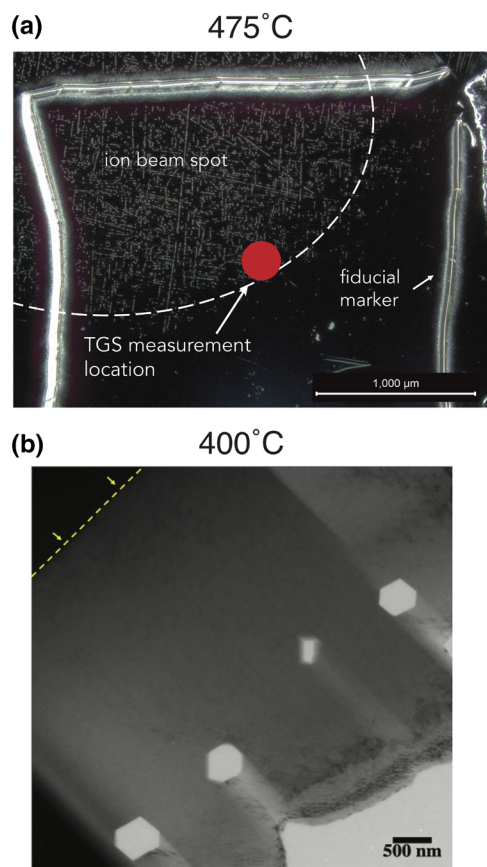


Fig. 5. (a) Post-exposure dark-field optical micrograph of self-ion irradiated pure copper at 475°C. The laser alignment fiducial and surface reconstruction due to the ion beam are evident. (b) Low-magnification, bright-field TEM of self-ion irradiated copper at 400°C. Faceted voids approximately 500 nm in diameter (lighter regions) are observed near the defect generation peak, oriented to the single-crystal surface of the sample (indicated by the dashed yellow line).

same system. To understand why the expected evolution in SAW velocity was not observed, post-irradiation optical microscopy as well as FIB lift-out and TEM was conducted. Figure 5a shows a dark-field optical micrograph of the 475°C sample. In this image, the upper section of a square fiducial marker used for laser alignment during TGS testing is clearly visible. This fiducial was scribed into the sample surface prior to exposure. As the scribe lines strongly scatter the incident lasers, they are used to target the TGS measurement spot into the center of the fiducial. Also visible in this image is surface reconstruction caused by ion beam exposure at high temperature. This type of phenomenon is commonly observed for low-energy ion implantation and its presence in these conditions, although not expected a priori, is within reason.^{82–85} Post-exposure optical images of the other two samples showed a similar arrangement of features. As the ion beam spot is clearly misaligned from the center of the fiducial area, it was not located coincident with the laser measurement spot during exposure. Therefore, although each copper sample received on the order

of 100 dpa at one particular location, the TGS response was not being monitored at that particular location during in situ testing. Likely, the SAW velocity shown in Fig. 4 is representative of a region near to the edge of the ion beam spot which only received a small amount of ion flux in the tails of the Gaussian profile.

Figure 5b shows a low-magnification bright-field TEM image of the post-exposure microstructure of the 400°C sample in the center of the ion beam location. Here, large, faceted voids approximately 500 nm in diameter with facets aligned with the single-crystal sample surface are clearly evident at a depth of 3–4 μm from the surface. This location corresponds to the peak defect generation regime at this ion beam energy.⁶⁸ This microstructure is consistent with that observed previously by Dennett and coworkers.³¹ As this TEM sample was extracted from the ion beam spot and not the TGS measurement location, it lends support to the theory generated from optical microscopy, namely that these exposure conditions do indeed cause volumetric swelling but TGS measurements returned the evolution of material properties from a region experiencing significantly less exposure. Similar cross-sectional imaging of 425°C and 475°C samples shows a decrease in total swelling as temperature is increased. This behavior indicates that for this dose rate, above 400°C, thermal vacancy emission is high enough to hinder void growth.⁸⁶ Additional microscopy of the TGS-monitored region on all samples will be conducted in the future to confirm the presence and type of defects in the lower-dose regime responsible for the stiffening and saturation observed here.

Following this series of TGS experiments, new protocols for ion beam–laser coincidence positioning have been put into place. These systems have since been shown to correct the misalignment observed here. With this correction, the dedicated I³TGS beamline is poised to be a powerful tool for monitoring material evolution under extremes of temperature and ion irradiation in the future.

FUTURE DIRECTIONS

The ability to use either passive or active listening to monitor the effects of ionizing radiation on materials has great potential for future applications. Due to the simplicity and ease of set-up of the single-transducer AE system, it can be easily integrated into many ion beam modification research and development efforts. For example, the inclusion of a transducer during a Smart Cut process would allow beam parameters to be determined for new material systems beyond single crystals (Si,⁸⁷ SiC,⁸⁸ LiNbO₃⁸⁹), for new crystal orientations, or for differing layer thicknesses from a single experiment where cleavage is directly resolved in time. This implementation would save scores of ion

implantation runs and significantly reduce time to commercialization. In a similar manner, a multiple transducer system would yield detailed, three-dimensional insight into the microscale evolution of damage that occurs during exposure to any type of ionizing radiation. This could include the ability to determine large-scale blistering during noble gas implantation or tritium decay or cracking and failure during heavy ion irradiation or operation of a nuclear reactor.

In a complimentary fashion, active listening techniques can be used to track the detailed evolution of the thermal and elastic properties of a range of materials, both model and commercial. Future advancements in this technology will permit mapping of the property evolution as a function of location with 10s of micrometer resolution. It has been demonstrated in this work that TGS can be performed during ion irradiation and at high temperature, but this method could also be coupled with other more extreme stressors, such as mechanical strain, fatigue, laser heating, electrical biasing, plasma exposure, etc. In addition, considerable promise exists for using TGS as an in-service materials monitoring technique where frequent measurements of TGS-measurable properties could be correlated to material health. For example, TGS could be used to assess the embrittlement of large stainless steel components in nuclear reactors, which degrade due to spinodal decomposition,⁹⁰ or to monitor the copper and phosphorus precipitate distribution which embrittles pressure vessel steels.⁹¹

Although this work has focused on AE and TGS applications during ion beam irradiation, it is easy to see how these and other advanced listening characterization and testing techniques can be applied to a range of laboratory and real-world radiation environments.

CONCLUSION

In this work, we have described preliminary work applying two distinct acoustic methodologies for in situ material monitoring during ion beam irradiation. In a model metal and ceramic, passive acoustic emission (AE) monitoring records a wealth of information simply by mounting samples to a piezoelectric transducer during exposure. In a model metal at high temperatures, active transient grating spectroscopy (TGS) tracks the evolution of radiation-induced defects by their changes on the elastic and acoustic properties of the material. While the exact natures of induced defect and damage events warrant further study for both of the methodologies used here, the temporal record of these events provides a map through which further investigation may be precisely targeted in both applied fluence and time. The application of these technologies is mature and minimal work is

necessary to incorporate some modality of acoustic monitoring into a range of in situ ion beam and other radiation environments.

ACKNOWLEDGEMENTS

The authors would like to thank Dan Buller, George Burns, and Stuart Van Deusen for their assistance and Trevor Clark for useful discussions. The time of N.M.H., B.L.B., and K.H. was fully supported by the U.S. Department of Energy, Office of Basic Energy Sciences, Division of Materials Sciences and Engineering. This work was supported in part by the MIT-SUTD International Design Center (IDC). This work was partially supported by the U.S. Department of Energy, Office of Nuclear Energy under DOE Idaho Operations Office Contract DE-AC07-051D14517 as part of a Nuclear Science User Facilities experiment. This work was performed, in part, at the Center for Integrated Nanotechnologies, an Office of Science User Facility operated for the U.S. Department of Energy (DOE) Office of Science. Sandia National Laboratories is a multimission laboratory managed and operated by National Technology & Engineering Solutions of Sandia, LLC, a wholly owned subsidiary of Honeywell International, Inc., for the U.S. DOE's National Nuclear Security Administration under Contract DE-NA-0003525. The views expressed in the article do not necessarily represent the views of the U.S. DOE or the United States Government.

ELECTRONIC SUPPLEMENTARY MATERIAL

The online version of this article (<https://doi.org/10.1007/s11837-019-03898-7>) contains supplementary material, which is available to authorized users.

REFERENCES

1. T. Allen, J. Busby, M. Meyer, and D. Petti, *Mater. Today* 13, 14 (2010).
2. S.J. Zinkle and G.S. Was, *Acta Mater.* 61, 735 (2013).
3. A. Jacobs, G. Cieslewski, A.D. George, A. Gordon-Ross, and H. Lam, *ACM Trans. Reconfig. Technol. Syst.* 5, 21:1 (2012).
4. J. Gonzalo, D. Domínguez, and D. López, *Prog. Aerosp. Sci.* 70, 28 (2014).
5. E. Keegan, M.J. Kristo, K. Toole, R. Kips, and E. Young, *Anal. Chem.* 88, 1496 (2016).
6. I. Yamada, J. Matsuo, N. Toyoda, T. Aoki, and T. Seki, *Curr. Opin. Solid State Mater. Sci.* 19, 12 (2015).
7. B.N. Singh, A.J.E. Foreman, and H. Trinkaus, *J. Nucl. Mater.* 249, 103 (1997).
8. K. Farrell, T.S. Byun, and N. Hashimoto, *J. Nucl. Mater.* 335, 471 (2004).
9. X. Xiao, Q. Chen, H. Yang, H. Duan, and J. Qu, *J. Nucl. Mater.* 485, 80 (2017).
10. K. Shiba and A. Hishinuma, *J. Nucl. Mater.* 283–287, 474 (2000).
11. G.A. Cottrell, R. Kemp, H.K.D.H. Bhadeshia, G.R. Odette, and T. Yamamoto, *J. Nucl. Mater.* 367–370, 603 (2007).

12. M.L. Jenkins and M.A. Kirk, *Characterisation of Radiation Damage by Transmission Electron Microscopy* (CRC Press, Boca Raton, 2000).
13. C.M. Barr, N. Li, B.L. Boyce, and K. Hattar, *Appl. Phys. Lett.* 112, 181903 (2018).
14. Z. Jiao and G.S. Was, *Acta Mater.* 59, 1220 (2011).
15. C.M. Barr, G.A. Vetterick, K.A. Unocic, K. Hattar, X.-M. Bai, and M.L. Taheri, *Acta Mater.* 67, 145 (2014).
16. C. Lu, T. Yang, K. Jin, N. Gao, P. Xiu, Y. Zhang, F. Gao, H. Bei, W.J. Weber, K. Sun, Y. Dong, and L. Wang, *Acta Mater.* 127, 98 (2017).
17. G.S. Was, Z. Jiao, E. Getto, K. Sun, A.M. Monterrosa, S.A. Maloy, O. Anderoglu, B.H. Sencer, and M. Hackett, *Scri. Mater.* 88, 33 (2014).
18. S.J. Zinkle and L.L. Snead, *Scri. Mater.* 143, 154 (2018).
19. E. Getto, K. Sun, A.M. Monterrosa, Z. Jiao, M.J. Hackett, and G.S. Was, *J. Nucl. Mater.* 480, 159 (2016).
20. E. Getto, K. Sun, S. Taller, A.M. Monterrosa, Z. Jiao, and G.S. Was, *J. Nucl. Mater.* 477, 273 (2016).
21. P. Hosemann, C. Shin, and D. Kiener, *J. Mater. Res.* 30, 1231 (2015).
22. A. Reichardt, A. Lupinacci, D. Frazer, N. Bailey, H. Vo, C. Howard, Z. Jiao, A.M. Minor, P. Chou, and P. Hosemann, *J. Nucl. Mater.* 486, 323 (2017).
23. P. Hosemann, *Scri. Mater.* 143, 161 (2018).
24. S.J. Dillon, D.C. Bufford, G.S. Jawaharram, X. Liu, C. Lear, K. Hattar, and R.S. Averback, *J. Nucl. Mater.* 490, 59 (2017).
25. B. Wang, M.A. Haque, V. Tomar, and K. Hattar, *MRS Commun.* 7, 595 (2017).
26. K.H. Matlack, J.J. Wall, J.-Y. Kim, J. Qu, L.J. Jacobs, and H.-W. Viehriig, *J. Appl. Phys.* 111, 054911 (2012).
27. K.H. Matlack, J.-Y. Kim, J.J. Wall, J. Qu, L.J. Jacobs, and M.A. Sokolov, *J. Nucl. Mater.* 448, 26 (2014).
28. J. Etoh, M. Sagisaka, T. Matsunaga, Y. Isobe, F.A. Garner, P.D. Freyer, Y. Huang, J.M.K. Wiezorek, and T. Okita, *J. Nucl. Mater.* 440, 500 (2013).
29. R.A. Duncan, F. Hofmann, A. Vega-Flick, J.K. Eliason, A.A. Maznev, A.G. Every, and K.A. Nelson, *Appl. Phys. Lett.* 109, 151906 (2016).
30. F. Hofmann, D. Nguyen-Manh, M.R. Gilbert, C.E. Beck, J.K. Eliason, A.A. Maznev, W. Liu, D.E.J. Armstrong, K.A. Nelson, and S.L. Dudarev, *Acta Mater.* 89, 352 (2015).
31. C.A. Dennett, K.P. So, A. Kushima, D.L. Buller, K. Hattar, and M.P. Short, *Acta Mater.* 145, 496 (2018).
32. G. Vizkelethy, B.L. Doyle, D.K. Brice, P.E. Dodd, M.R. Shaneyfelt, and J.R. Schwank, *Nucl. Instrum. Methods Phys. Res. B* 231, 467 (2005).
33. J.A. Hinks, *Nucl. Instrum. Methods Phys. Res. B* 267, 3652 (2009).
34. S. Miro, G. Velisa, L. Thomé, Y. Trocellier, P. and Seruys, A. Debelle, and F. Garrido, *J. Raman Spectrosc.* 45, 481 (2014).
35. K. Hattar, D.C. Bufford, and D.L. Buller, *Nucl. Instrum. Methods Phys. Res. B* 338, 56 (2014).
36. G. Greaves, A.H. Mir, R.W. Harrison, M.A. Tunes, S.E. Donnelly, and J.A. Hinks, *Nucl. Instrum. Methods Phys. Res. A* 931, 37 (2019).
37. J.A. Hudson, R.S. Nelson, and R.J. McElroy, *J. Nucl. Mater.* 65, 279 (1977).
38. K. Tai, R.S. Averback, P. Bellon, Y. Ashkenazy, and B. Stumphy, *J. Nucl. Mater.* 422, 8 (2012).
39. S. Özerinç, R.S. Averback, and W.P. King, *JOM* 68, 2737 (2016).
40. G.S. Jawaharram, P.M. Price, C.M. Barr, K. Hattar, R.S. Averback, and S.J. Dillon, *Scri. Mater.* 148, 1 (2018).
41. D. Lockner, *Int. J. Rock Mech. Min. Sci.* 30, 883 (1993).
42. E. Andò, S.A. Hall, G. Viggiani, J. Desrues, and P. Bésuelle, *Acta Geotech.* 7, 1 (2012).
43. M.D. Ingraham, K.A. Issen, and D.J. Holcomb, *Acta Geotech.* 8, 645 (2013).
44. D. Adliene, L. Pranevicius, and A. Ragauskas, *Nucl. Instrum. Methods Phys. Res.* 209–210, 357 (1983).
45. T. Kambara, Y. Kanai, T.M. Kojima, Y. Nakai, A. Yoneda, K. Kageyama, and Y. Yamazaki, *Nucl. Instrum. Methods Phys. Res. B* 164–165, 415 (2000).
46. T. Kambara, *Nucl. Instrum. Methods Phys. Res. B* 230, 601 (2005).
47. A.A. Maznev, K.A. Nelson, and J.A. Rogers, *Opt. Lett.* 23, 1319 (1998).
48. F. Hofmann, M.P. Short, and C.A. Dennett, *MRS Bull.* 44, 392 (2019).
49. C.A. Dennett, D.L. Buller, K. Hattar, and M.P. Short, *Nucl. Instrum. Methods Phys. Res. B* 440, 126 (2019).
50. H.N.G. Wadley, C.B. Scruby, and J.H. Speake, *Int. Met. Rev.* 25, 41 (1980).
51. H.L. Dunegan, C.A. Tatro, and D.O. Harris, *Acoustic emission research*, Tech. Rep. UCID-4868 (Lawrence Radiation Laboratory, University of California, Livermore, 1964).
52. H.L. Dunegan, D.O. Harris, and A.S. Tetelman, Detection on fatigue crack growth by acoustic emission techniques, in *Proceedings of the Seventh Symposium on Nondestructive Evaluation of Components and Materials in Aerospace, Weapons Systems, and Nuclear Applications* (1969).
53. M. Huang, L. Jiang, P.K. Liaw, C.R. Brooks, R. Seeley, and D.L. Klarstrom, *JOM* 50, 1 (1998).
54. C.U. Grosse and M. Ohtsu, *Acoustic Emission Testing* (Springer, Berlin, 2008).
55. K.R. Shah and J.F. Labuz, *J. Geophys. Res. Solid Earth* 100, 15527 (1995).
56. W.A. Olsson and D.J. Holcomb, *Geophys. Res. Lett.* 27, 3537 (2000).
57. P. Baud, E. Klein, and T.F. Wong, *J. Struct. Geol.* 26, 603 (2004).
58. J. Fortin, S. Stanchits, G. Dresen, and Y. Guéguen, *J. Geophys. Res. Solid Earth* 111, B10203 (2006).
59. Z. Li and S.P. Shah, *Mater. J.* 91, 372 (1994).
60. C. Grosse, H. Reinhardt, and T. Dahm, *NDT E Int.* 30, 223 (1997).
61. D.-J. Yoon, W.J. Weiss, and S.P. Shah, *J. Eng. Mech.* 126, 273 (2000).
62. K. Ohno and M. Ohtsu, *Constr. Build. Mater.* 24, 2339 (2010).
63. F. Schubert, Basic principles of acoustic emission tomography, in *26th European Conference on Acoustic Emission Testing (EWGAE)* (2004).
64. J.A. Johnson, A.A. Maznev, M.T. Bulsara, E.A. Fitzgerald, T.C. Harman, S. Calawa, C.J. Vineis, G. Turner, and K.A. Nelson, *J. Appl. Phys.* 111, 023503 (2012).
65. O.W. Käding, H. Skurk, A.A. Maznev, and E. Matthias, *Appl. Phys. A* 61, 253 (1995).
66. C.A. Dennett and M.P. Short, *J. Appl. Phys.* 123, 215109 (2018).
67. C.A. Dennett, P. Cao, S.E. Ferry, A. Vega-Flick, A.A. Maznev, K.A. Nelson, A.G. Every, and M.P. Short, *Phys. Rev. B* 94, 214106 (2016).
68. J.F. Ziegler, M.D. Ziegler, and J.P. Biersack, *Nucl. Instrum. Methods Phys. Res. B* 268, 1818 (2010).
69. C.M. Jimenez, L.F. Lowe, E.A. Burke, and C.H. Sherman, *Phys. Rev.* 153, 735 (1967).
70. B. Wang, Y. Yu, I. Pignatelli, G. Sant, and M. Bauchy, *J. Chem. Phys.* 143, 024505 (2015).
71. K. Azumi, S. Ishiguro, T. Mizuno, and M. Seo, *J. Electroanal. Chem.* 347, 111 (1993).
72. J. Čížek, O. Melikhova, P. Dobroň, and P. Hruška, *Int. J. Hydrog. Energy* 42, 22460 (2017).
73. M. Hiraga, G. Izawa, and K. Yoshihara, *Nucl. Instrum. Methods Phys. Res. B* 51, 163 (1990).
74. T. Schober, J. Golczewski, R. Lässer, C. Dieker, and H. Trinkaus, *Z. Phys. Chem.* 147, 161 (1986).
75. J.M. Jungk, B.L. Boyce, T.E. Buchheit, T.A. Friedmann, D. Yang, and W.W. Gerberich, *Acta Mater.* 54, 4043 (2006).
76. J. Friedel, *Philos. Mag.* 44, 444 (1953).
77. D.M. Parkin, J.A. Goldstone, H.M. Simpson, and J.M. Hemsley, *J. Phys. F Met. Phys.* 17, 577 (1987).
78. N. Li, K. Hattar, and A. Misra, *J. Nucl. Mater.* 439, 185 (2013).

79. B.D. Wirth, V.V. Bulatov, and T. de la Rubia, *J. Eng. Mater. Technol.* 124, 329 (2002).
80. D.O. Thompson and D.K. Holmes, *J. Appl. Phys.* 27, 713 (1956).
81. D.P.H. Hassleman and R.M. Fulrath, *J. Am. Ceram. Soc.* 47, 52 (1964).
82. I.H. Wilson, *J. Appl. Phys.* 53, 1698 (1982).
83. G. Carter and V. Vishnyakov, *Phys. Rev. B* 54, 17647 (1996).
84. U. Valbusa, C. Boragno, and F. Bautier de Mongeot, *J. Phys. Condens. Matter.* 14, 8153 (2002).
85. O. R. de la Fuente, M.A. González, and J.M. Rojo, *Phys. Rev. B* 63, 085420 (2001).
86. L.D. Glowinski, J.M. Lanore, C. Fiche, and Y. Adda, *J. Nucl. Mater.* 61, 41 (1976).
87. M. Bruel, *Electron. Lett.* 31, 1201 (1995).
88. L. Di Cioccio, Y. Le Tiec, F. Letertre, C. Jaussaud, and M. Bruel, *Electron. Lett.* 32, 1144 (1996).
89. R.H. Olsson, K. Hattar, S.J. Homeijer, M. Wiwi, M. Eichenfield, D.W. Branch, M.S. Baker, J. Nguyen, B. Clark, T. Bauer, and T.A. Friedmann, *Sens. Actuator A Phys.* 209, 183 (2014).
90. S.A. Aldajani, B.R. Dacus, C.A. Dennett, M.G. Burke, K. Mukahiwa, K. Anglin, J.J. Wall, T.S. Byune, M.P. Short, Non-destructively detecting LWR structural material embrittlement using transientgrating spectroscopy, in *19th International Conference on Environmental Degradation of Materials in Nuclear Power Systems - Water Reactors* (2019).
91. B. Gurovich, Y.N. Korolev, E.A. Kuleshova, Y.A. Nikolaev, Y.I. Shtrombakh, Irradiation embrittlement of reactor pressure vessel steels due to mechanisms other than radiation hardening, in *Effects of Radiation on Materials: 18th International Symposium* (1999).

Publisher's Note Springer Nature remains neutral with regard to jurisdictional claims in published maps and institutional affiliations.